

Extremely Slow Photoconductivity Response of $\text{CH}_3\text{NH}_3\text{PbI}_3$ Perovskites Suggesting Structural Changes under Working Conditions

Ronen Gottesman,[†] Eynav Haltzi,[†] Laxman Gouda, Shay Tirosh, Yaniv Bouhadana, and Arie Zaban*

Department of Chemistry, Center for Nanotechnology & Advanced Materials, Bar Ilan University, Ramat Gan 52900, Israel

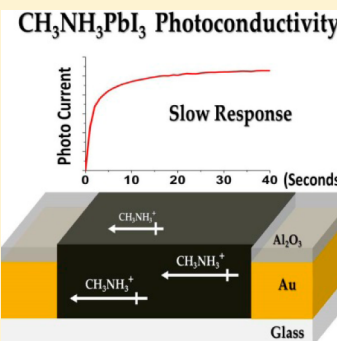
Edoardo Mosconi and Filippo De Angelis

Computational Laboratory for Hybrid/Organic Photovoltaics (CLHYO), CNR-ISTM, Via Elce di Sotto 8, I-06123 Perugia, Italy

Supporting Information

ABSTRACT: Photoconductivity measurements of $\text{CH}_3\text{NH}_3\text{PbI}_3$ deposited between two dielectric-protected Au electrodes show extremely slow response. The $\text{CH}_3\text{NH}_3\text{PbI}_3$, bridging a gap of ~ 2000 nm, was subjected to a DC bias and cycles of 5 min illumination and varying dark duration. The approach to steady-state photocurrent lasted tens of seconds with a strong dependence on the dark duration preceding the illumination. On the basis of DFT calculations, we propose that under light + bias the methylammonium ions are freed to rotate and align along the electric field, thus modifying the structure of the inorganic scaffold. While ion alignment is expected to be fast, the adjustment of the inorganic scaffold seems to last seconds as reflected in the extremely slow photoconductivity response. We propose that under working conditions a modified, photostable, perovskite structure is formed, depending on the bias and illumination parameters. Our findings seem to clarify the origin of the well-known hysteresis in perovskite solar cells.

SECTION: Energy Conversion and Storage; Energy and Charge Transport



O riginating from research on solution-processable semiconductors, photovoltaic devices based on methylammonium lead trihalide perovskite absorbers ($\text{CH}_3\text{NH}_3\text{PbX}_3$ or MAPbX_3 , where $X = \text{Br}, \text{Cl}, \text{I}$) have reported certified efficiencies as high as 17.9%. Whereas the first reported perovskite-sensitized solar cell back in 2009 showed 3.8% efficiency in a dye-sensitized solar cell (DSSC) configuration,¹ these absorbers were implemented in three other device architectures, all yielding more than 15% efficiency.^{2–4} The structural diversity ranged between meso-superstructures² (replacing the nanoporous TiO_2 ^{5,6} with an alumina scaffold) to mesoscopic³ and planar junction⁴ devices. In the meso-superstructure and planar junction devices a mixed halide perovskite ($\text{MAPbI}_{3-x}\text{Cl}_x$) was used. The band-gap and crystal structure remained the same as when using the plain MAPbI_3 .⁷ However, for reasons that are still under investigation, properties such as charge-carrier diffusion lengths and PL lifetime are greatly enhanced in the $\text{MAPbI}_{3-x}\text{Cl}_x$.^{8,9} The fact that the physics of each of these three devices is inherently different is an indication that MAPbX_3 materials are very unique.^{10,11} The hybrid perovskites are ambipolar,^{12–14} can efficiently transport both electrons and holes,^{15–17} and possess unusually long electron and hole diffusion lengths.^{8,18} However, most of the fundamental questions concerning why these materials are so effective at generating and transporting photocurrents remain unanswered. Despite the rapid increase

in MAPbX_3 solar cell efficiency associated with device evolution, optimization and full characterization of devices is still a major assignment for researchers to accomplish.^{10,19,20} While advanced characterization^{7,21–23} of MAPbX_3 solar cells is already in progress around the world, photophysical studies of isolated perovskite thin films under solar cell working conditions are still rare.

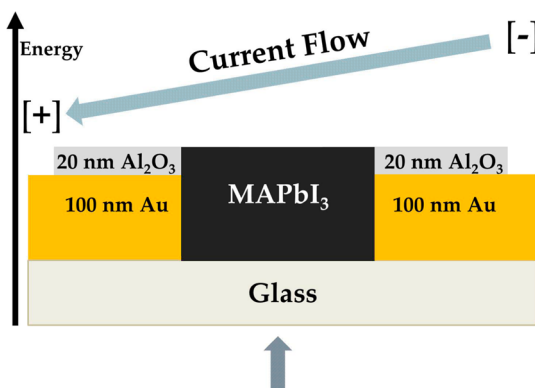
In this work, we studied the photoconductivity of MAPbI_3 deposited between two gold electrodes spaced ~ 2000 nm apart. The novelty of the device is that it is a symmetrical system, without any intrinsic selective contacts (electron and hole transport materials). A constant DC bias was applied between the two dielectric-protected Au electrodes (20 nm of Al_2O_3), while the film was illuminated from the bottom, as illustrated in Scheme 1. A film of MAPbI_3 was deposited by spin coating into the gap and then annealed and photophysically characterized. Figure 1a shows a high-resolution scanning electron microscope (HRSEM) image of the empty gap of ~ 1500 nm before MAPbI_3 deposition. The gap was created using a focused ion beam (FIB), utilizing Gallium ions for the patterning (The patterning's role is to create two closely spaced electrodes and is described fully in the Experimental Methods and Computa-

Received: July 2, 2014

Accepted: July 22, 2014

Published: July 22, 2014



Scheme 1. Illustration of the Measurement System^a

^aMAPbI₃ is deposited in the gap between two dielectric-protecting layers of Al₂O₃ onto two Au electrodes. A DC bias is applied between the working and the counter electrodes while the gap is illuminated from the bottom.

tional Details.) The goal of the insulating Al₂O₃ top layer was to prevent electrical interaction between the deposited MAPbI₃ and the gold's top surface. Moreover, when depositing MAPbI₃ directly on gold electrodes without any top layer of Al₂O₃, the perovskite film covered the gap and the surface of the adjacent electrodes, making it hard to visibly distinguish if the perovskite actually penetrated the gap efficiently (Figure S1 in the Supporting Information). Surprisingly, we have learned that the MAPbI₃ solution does not wet the Al₂O₃ layer well, causing the film to settle mostly inside the gap, as seen in Figure 1b,c (gap width is ~2000 nm). Because of the fact that the MAPbI₃ formation was mostly constrained to the gap, no visible evidence of the perovskite (black color) was observed on the device. Several gap widths in the range of 500–2500 nm were measured in this study. However, complete filling of the gap was successful only in the wider ones. Thus, the current report utilizes data of gaps that are ~2000 nm apart.

Prior to the deposition of the MAPbI₃, the FIB patterning was verified by connecting the setup to a potentiostat and sweeping through a wide range of biases, all showing null currents between the working and the counter electrodes (data not shown). The system is symmetrical and without any selective contacts, and so a DC bias was applied to create current flow. Measurements were done under a range of continuous DC biases. The MAPbI₃ filled gap was illuminated for 5 min with white light at 1 sun intensity; then, the light was turned off for between 1 and 60 s, each time for a different duration. The light was then turned on again for 5 min. This process continued until a full current versus time (*i*-*t*) profile was obtained, comprised from many dark/light cycles (each cycle referring to a different amount of "dark time" and then held under light for 5 min).

Our system was designed to study the photoconductivity of MAPbI₃. In a general photoconductivity measurement when the light is turned on, a typical spike followed by a decay or a direct rise is observed. In some of the studied gap systems, we observed the spike followed by a decay, as seen in Figure 2a,b. (This case will be designated as spike → decay.) However, in other gap systems, in which the perovskite was deposited in the same way, we observed currents slowly rise directly to a steady state without an initial spike, as seen in Figure 2c,d. (This case will be designated as direct rise.) It is important to note that changing the magnitude or the sign of the bias did not shift

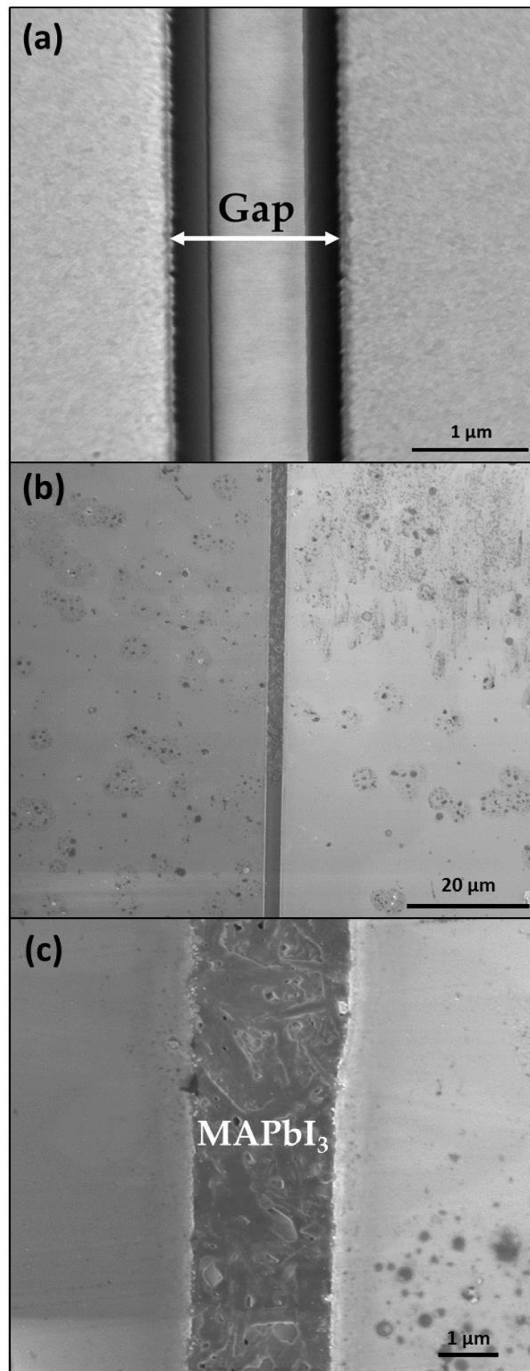


Figure 1. (a) HRSEM image of the gap before MAPbI₃ deposition, showing an empty gap created using the focused ion beam. (b) Low-magnification image of the MAPbI₃ filled gap, showing that the top of the Al₂O₃ layer is visibly clear of any perovskite. (c) High magnification of a section in panel b, showing a dense looking MAPbI₃ film deposited between the gap walls.

between the two cases (opposite photoconductivity responses). However, the common phenomenon to both cases is the very long time scales it takes for the current to reach a steady state. This behavior is also dependent on the amount of time the system is in the dark prior to reillumination. We attribute this phenomenon to dipole alignment under bias + light of MA in the MAPbI₃. We will discuss other possible mechanisms, and explain why, in our opinion, they are not suitable in this

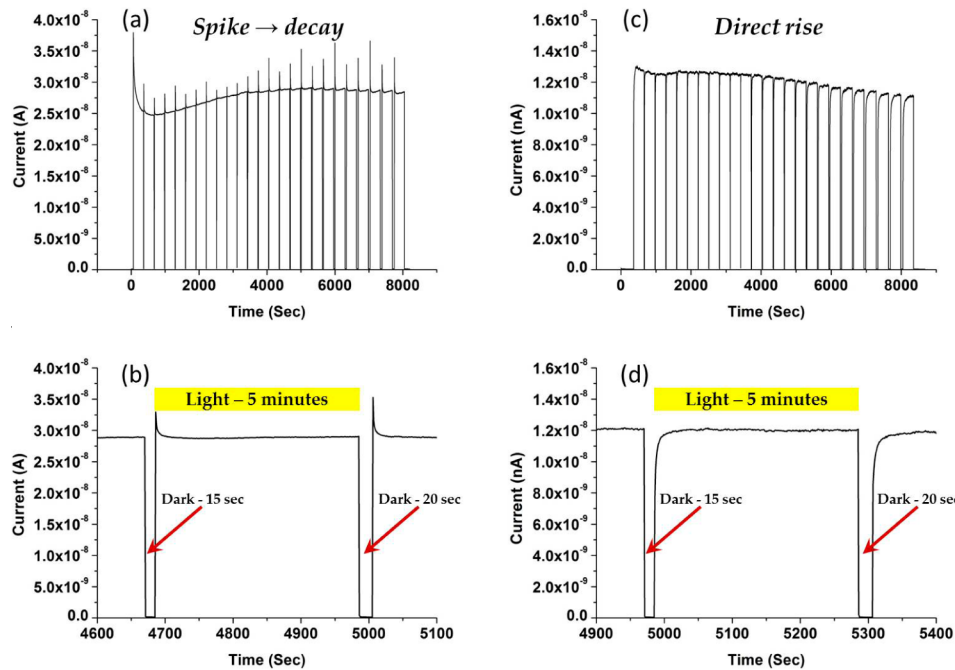


Figure 2. (a,c) Full $i-t$ profiles for the spike \rightarrow decay and direct rise cases, showing the full range of cycles. The dark times are visible by the drop in the current when the light was turned off (each time for a different period) and then turned on for 5 min. (b,d) 500 s sections taken from panels a and c, respectively, showing a dark time of 15 s before illuminating for 5 min, then the light is turned off again for 20 s, and so on.

circumstance, leaving dipole alignment as the most probable mechanism.

Figure 2a,c shows examples of $i-t$ profiles for the two photoconductivity responses (applied bias = 0.1 V), showing the full collection of cycles, with dark times of 1–60 s: 1 s resolution for the short dark durations (1–15 s) and 5 s increments for the dark of 20–60 s. We note that the preset dark durations were set randomly rather than ordered to increase or decrease during the measurement. Figure 2b,d shows sections taken from the full measurements shown in Figure 2a,c (respectively), displaying a 5 min illumination period preceded by a dark time of 15 s. After 5 min, the light is turned off again for 20 s and so on.

The $i-t$ profiles showing the current's decay/rise to steady state upon illumination were taken from all of the cycles and plotted one on top of another for comparison. The plots presented in Figure 3 were normalized to zero at steady-state current. For the case of spike \rightarrow decay, we present the results of two biases: Figure 3a relating to 0.1 V and Figure 3b to 0.3 V. (See also Figure S2 in the Supporting Information for log presentation.) The case of direct rise is presented in a similar way with Figure 3d,e presenting the different cycles with applied biases of 0.1 and 0.3 V, respectively (log presentation in Figure S2 in the Supporting Information). The negative current signs in Figure 3d,e have no physical meaning and are derived from the normalization. The curves are defined by the dark time that preceded its illumination period.

It is clear from Figure 3 that for both cases the amount of time it takes to reach steady-state currents is on the order of many seconds. Moreover, the time it takes to reach steady state is dependent on the dark duration prior to reillumination. In other words, as the dark period is longer, the decay is slower. This very surprising finding shows that the decays are on the order of many seconds, reaching even to tens of seconds in specific cases. These values are enormous compared with other

well-known semiconductors used in photovoltaic devices, and as far as we know, this is the first time it is shown in an isolated MAPbX_3 thin film, without selective-contacts. In addition, the magnitude of the electric field (the DC bias) induced on the MAPbI_3 also affects the decay times. As the bias increased, the decays became slower. This can be seen clearly comparing Figure 3a,b, or d,e, where in Figure 3b,e, the bias magnitude is three times higher. When we applied higher biases, such as 1 V, the effect was even stronger however much nosier (Figure S3 in the Supporting Information).

Figure 3c,f shows for both cases the time (in seconds) it took for the current to reach steady state versus the preceding dark duration. It is shown that the dark duration affects the time required for the system to reach steady state under illumination. Up to ~ 30 s, the relaxation time to steady-state photocurrent increases with the preceding dark length. For longer dark periods, a plateau is observed, indicating that the system relaxes to its dark state within ~ 30 s. We note that Figure 3c,f present a decay to 5% of the initial peak value, which resembles decay rates rather than the absolute time. As can be seen from Figure 3a,b or d,e, the absolute decay time increases with the bias applied across the gap.

The observed current decays seem to be associated with changes in charge mobility; that is, upon illumination the photoconductivity slowly decreases (spike \rightarrow decay) or increases (direct rise) to a steady-state value with illumination time. The fact that longer dark durations prolong this decay/rise process suggests that the material somehow endures changes under illumination, while in the dark it returns to a relaxed state. The results suggest that the transition between the proposed states is very slow: tens of seconds. These time scales are very uncommon, in both the dark and light.

Before we progress along this hypothesis, we need to examine two very straightforward possibilities. First, the MAPbI_3 interacts somehow with the alumina layer, causing

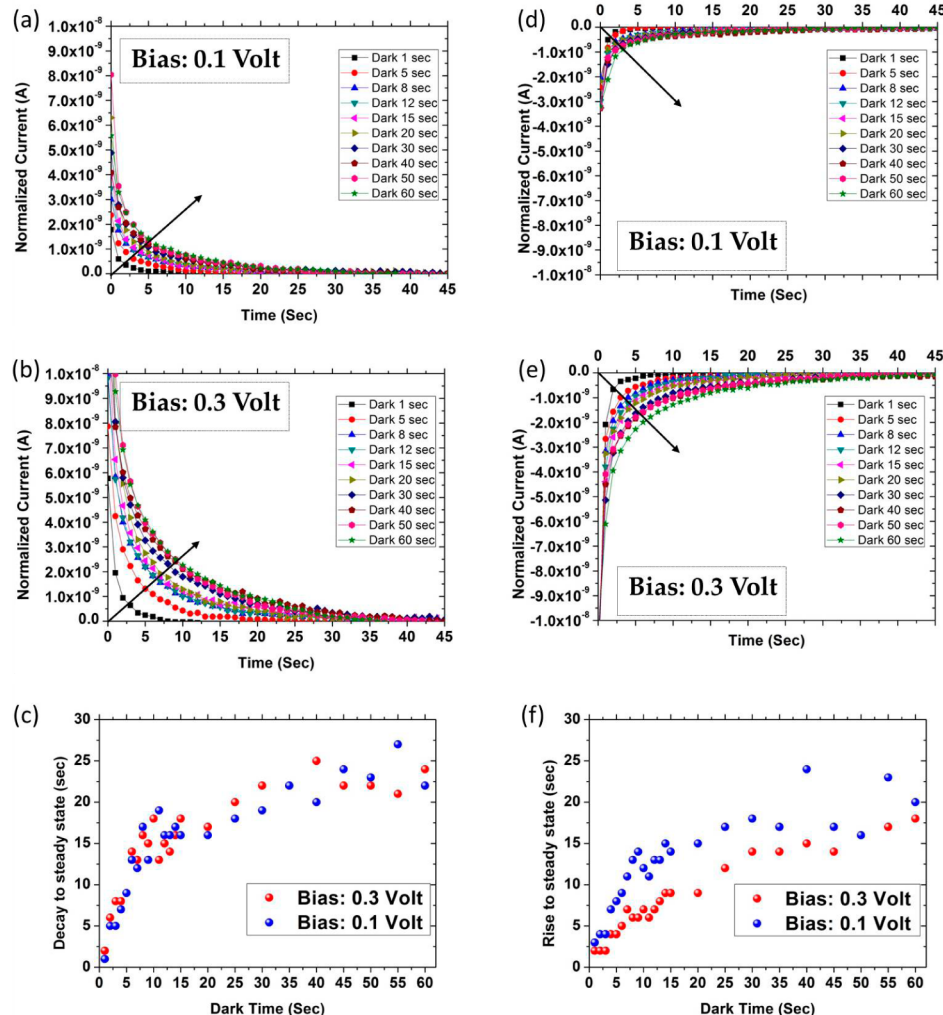


Figure 3. (a,b) spike → decay and (d,e) direct rise normalized current decay plots to a designated value of 0 Ampere (steady state current) of different dark times. (a,d) Applied bias of 0.1 V and (b,e) 0.3 V. (The black arrows point from short to long dark durations.) (c,f) Plots showing the time (in seconds) it takes the current to decay to a value of 5% from the average peak value at each bias versus the dark time before each illumination period.

long-lived traps that delay these decay times. As a result, the same measurements were carried out without a top layer of Al_2O_3 , yielding the same observed decays. The second possibility relates to the spike → decay case only thus seeming irrelevant. Nevertheless, we examined it. The notion was a possible charge accumulation in the film occurring under illumination, which slowly builds up with time and causes the observed decays. To find out, we integrated the area underneath the current decay curve yielding charge. The charge was then divided by the volume of the MAPbI_3 film (estimated by prior knowledge of the dimensions of the gap). The calculated numbers were enormous, ranging in some cases between 0.1 and 1 electrons per unit cell of MAPbI_3 . Because of the magnitude of these numbers and the fact that it does not explain the direct rise case, we abandoned the possibility of charge build-up.

Three mechanisms can be suggested for the observed photoconductivity responses: (a) migration of the methylammonium ions throughout the film under illumination and electric fields, (b) photoinduced traps for charge carriers in the MAPbI_3 (within the bulk or near the surface/interface), and (c) dipole alignment in the material induced by a combination of

illumination and the bias applied across the MAPbX_3 (a material that has already been observed to possess ferroelectric properties²⁴). However, when witnessing two opposite behaviors of decreased/increased photoconductivity in the same material (different devices), the first two mechanisms are less probable. Migration of ions is unlikely because the ions will always migrate toward the negative electrode, resulting in only one photoconductivity response. In addition, photoinduced traps are also unlikely because they cannot explain the case of increased photoconductivity (direct rise) over time. We propose dipole alignment in the material induced by a combination of light + bias as the most probable scenario that occurs in the MAPbX_3 , and we will elaborate it in length. The three mechanisms were also discussed by Snaith et al., in reference to the widely observed hysteresis phenomenon in MAPbX_3 solar cells,²⁵ but the experimental data were not sufficient to discriminate between the mechanisms.

In light of the previous discussion, hypothesis c was investigated, that is, the chance of a structural change associated with orientation of the methylammonium dipoles mediated by light absorption. In the low-temperature limit, that is, for the orthorhombic phase, the MA cations show an ordered

orientation.²⁶ For the high-temperature cubic phase of MAPbI_3 , a fast rotational dynamics of the MA cations was observed, with a characteristic picosecond time scale.²⁷ We note that even without any external perturbation (light or bias) the MA cations exhibit a dynamic disorder for the room-temperature tetragonal phase of the MAPbI_3 perovskite.²⁸

To check whether light absorption could alter the possible preferred orientation of the MA cations, we have performed DFT calculations, both scalar relativistic (SR) and including spin-orbit coupling (SOC); see the Experimental Methods and Computational Details later. We considered two MAPbI_3 structures, one similar to the lowest energy structure previously characterized by some of us,²⁹ hereafter structure 1 (dark structure), and one obtained by a ferroelectric arrangement of the methylammonium cations,²⁴ hereafter structure 2 (light + bias structure); see Figure 4. Structure 1 is characterized by the

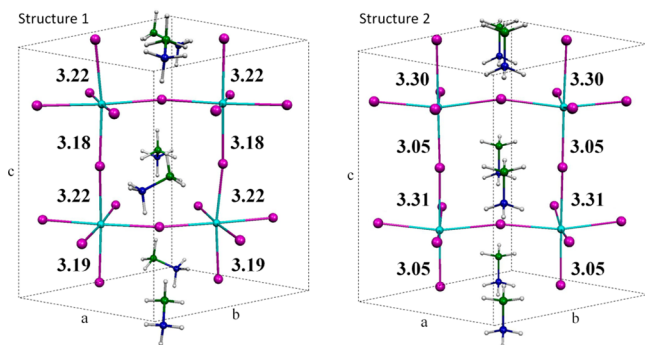


Figure 4. Optimized geometrical structure for systems 1 and 2, along with apical I–Pb bond lengths (angstroms). Notice the different arrangement of the methylammonium ions in 1 and 2.

methylammonium cations lying slightly bent ($\sim 30^\circ$ angle) with respect to the ab plane (Figure 4), with a twisted head-to-head arrangement and a sizable tilting of the PbI_6 octahedra, as experimentally found,^{24,30} while in structure 2 the MA cations are strongly oriented along the crystallographic c axis, with no octahedra tilting. Notice that the two considered structures are simply chosen here to sample partially disordered and strongly ordered MA configurations. Our calculations, performed without any symmetry constraint on a 48 atoms unit cell, reveal for both structure 1 and 2 an atomic arrangement consistent with the $I4cm$ space group, with a sizable off centering of the Pb atoms, more pronounced for structure 2; see Figure 4.

Upon relaxation of atomic and lattice parameters, structure 2 is predicted to be less stable than 1 by 0.37 eV. The calculated cell parameters are in both cases within 1 to 2% of the corresponding experimental data,²⁴ but notably in structure 2 an expansion of the a – b parameters is found, associated with a slight contraction of the c lattice dimension; see Table 1.

Structures 1 and 2 are characterized by a similar band gap; inclusion of SOC leads in both cases to a reduction of the band gap³¹ with the nontilted structure 2 showing a further band-gap

reduction by SOC.³² Despite the fact that SOC-DFT calculated band gaps are smaller than experimental values, we can confidently say that the two structures have roughly the same band gap within ± 0.05 eV. Relativistic GW calculations on MAPbI_3 indeed confirm that SOC-DFT band gaps qualitatively follow the trend of the more accurate SOC-GW results.^{33,34}

To provide insight into a possible light-induced methylammonium rearrangement mechanism, we simulated the lowest triplet state for structures 1 and 2, obtained by unpairing one electron from the ground state, and calculated the binding energy of a methylammonium cation to structures 1 and 2 in the ground state and in the lowest triplet state within SR-DFT. Our calculations indicate there is a decrease in the binding energy of the MA ions to the inorganic cage (by 0.07 eV) when going from the ground to the lowest triplet state. This binding energy reduction likely allows the cations to more freely rotate upon light excitation. Such binding energy decrease is originated by the $\text{I} \rightarrow \text{Pb}$ charge-transfer nature of the band-gap excitation (Figure 5), which depletes the negative charge

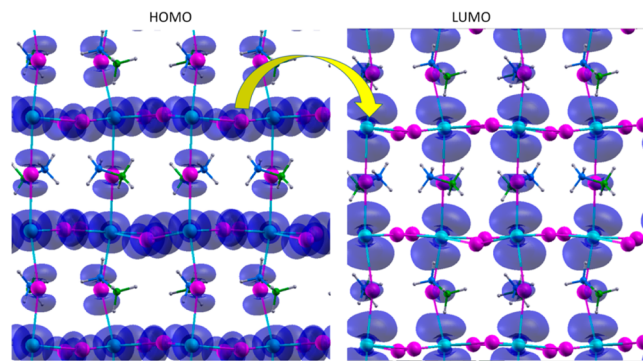


Figure 5. HOMO and LUMO states for structure 1 of MAPbI_3 calculated by SR-DFT. A displacement of charge from the I to the Pb atoms is calculated upon band-gap excitation (yellow arrow), leading to a decreased binding energy of the methylammonium cations to the inorganic cage.

carried by the iodine atoms. The MA cations, mainly interacting with the inorganic cage by hydrogen bonding to the iodine atoms, are therefore less tightly bound in the excited state than in the ground state and can more freely rotate under the action of the applied electric field. This mechanism could be related to the “photoferroic effect” proposed by Brivio et al.,³⁵ and it can be possibly associated with the exciton screening by collective orientational motion of the organic cations at room temperature, leading to almost free carriers, suggested by Even et al.³⁶

We have thus shown that the movement of the MA cations is likely to have a significant effect on the polarity of the MAPbI_3 , possibly causing a structural change to the inorganic framework of the material. These changes might take longer to follow the new dipole direction, although we still cannot estimate their time dynamics. The amount of dark time it takes for the MAPbI_3 to reach a relaxed state can be derived from Figure 3c,f, and it is ~ 30 s. If the material is reilluminated before full relaxation, the decay will be faster due to the fact that some dipoles are still aligned in the direction of the electric field.

As previously discussed, the photoconductivity can vary in two opposite directions, showing either the spike → decay (decreased photoconductivity) response or the direct rise (increased photoconductivity) response. As previously noted, these responses are sample specific; that is, for a given gap

Table 1. Calculated Lattice Parameters (Å), Relative Energies (eV), and Band Gaps (eV) by SR- and SOC-DFT

structure	a	b	c	rel. energy	E_g (SR)	E_g (SOC)
1	8.75	8.74	12.77	0.00	1.57	0.53
2	8.85	8.85	12.71	0.37	1.60	0.46

system we observe only one type of response. Consequently, we suggest that the observed phenomena are connected with the specific film deposition parameters. These highly subtle parameters control the specific structure or orientation of the polycrystalline film³⁷ with respect to the gold electrodes. At each specific structure or orientation, the photoconductivity response will depend on the collective alignment of the MA dipoles under light + bias. For some structures it will decrease, while others will experience an increase.

The long decays/rises shown in Figure 3, which we interpret as photo + bias-induced changes in photoconductivity, can shed light on the known hysteresis in the MAPbX_3 materials. This hysteresis is said to be related to device architecture and iV scan rate,²⁵ although its origin has not been fully understood. Furthermore, this effect is not detectable in dark measurements.³⁸ As we have shown here, the photoconductivity changes are very much dependent on the magnitude of the applied bias. (As the bias increased, the decays/rises were slower.) In a typical iV scan of a solar cell, the applied bias is swept in both directions, from forward bias to short-circuit and from short-circuit to forward bias. In one direction, the electric field is changing from high to low and then from low to high. In perovskite solar cells, it has been shown that the hysteresis gets more extreme as the scan rate is reduced. (It can still be significant at very slow scan rates.) Taking into account the fact that the MAPbX_3 may fully transforms to its so-called “new” structure in ~ 30 s, scanning the voltage causes a constant structural change due to the constant collective alignment of the MA dipoles. Therefore, the iV scan rate is a key factor; that is, when the rate is fast, the inorganic scaffold of the MAPbX_3 does not have sufficient time to adjust. This could reduce the transient change in photoconductivity, which would result in a reduced hysteresis. Our theory has been reinforced by Bisquert et al., who recently showed slow dynamic processes³⁹ and photoinduced giant dielectric constants⁴⁰ in MAPbX_3 solar cells. The authors’ hypothesis is that structural fluctuations depended on the MA freedom of rotation.

It has been shown in a perovskite solar cell that when holding the potential near V_{oc} , J_{sc} and the maximum power point (MPP) under light for long periods of time, the photocurrent reaches a steady state after many seconds.²⁵ This amount of time is on the same time scales as our observed changes in photoconductivity. The authors do show that after holding the potential near the MPP, an increase in the photo current occurs. However, when sweeping the applied bias after the light exposure at the MPP, the hysteresis was still strongly apparent.

In summary, we have designed a method to study MAPbI_3 perovskite films without selective contacts. Under a range of applied biases and preset dark and light times, we have measured the photoconductivity of MAPbI_3 . Noticeable are two opposite cases of decreased and increased photoconductivity occurring with time. The difference between the two cases is suggested to depend on exact film deposition parameters, which determine a specific structure or orientation of the polycrystalline film relative to the gold electrodes. The common phenomenon to both cases is the long time scales it takes to reach a steady-state current. In addition, the amount of time in the dark before reillumination affects the time to a steady state. We propose that under light + bias the methylammonium ions have enhanced rotational freedom and may align with the electric field, as indicated by DFT calculations. Our calculations also suggest a marginal band-gap variation upon cation alignment, which could be difficult to

reveal by optical spectroscopy. This alignment might be very fast, but the adjustment of the inorganic scaffold is much slower, seen as long time-scale changes in the photoconductivity. We propose that under solar cell working conditions the structure of the $\text{CH}_3\text{NH}_3\text{PbI}_3$ perovskite varies depending on the applied bias and/or the light intensity. This phenomenon can explain the long duration reported for cells to reach maximum power upon illumination (changes in illumination conditions) as well as the well-known hysteresis during iV scans (bias variation). It is also possible that the findings reported in this work explain the uniqueness of this material family with respect to photovoltaic applications.

■ EXPERIMENTAL METHODS AND COMPUTATIONAL DETAILS

Fabrication of the electrodes was done by deposition of Al_2O_3 /Au/Cr (thicknesses: 20/100/10 nm, respectively) in rectangular designs on top of a glass substrate using a mechanical mask. The rectangle’s dimensions were 25 mm \times 1 mm. Both ends of the rectangle were masked prior to the Al_2O_3 deposition to allow electrical contact with the Au layer. The gaps were created by a FIB (combined with a scanning electron microscope) to pattern a gap across each rectangle, resulting in a two separate electrodes spaced 500–2500 nm apart. The perovskite $\text{CH}_3\text{NH}_3\text{PbI}_3$ was prepared using a procedure described elsewhere.⁴¹ Methylammonium iodide ($\text{CH}_3\text{NH}_3\text{I}$) was synthesized by reacting methylamine (CH_3NH_2) solution (33 wt % in absolute ethanol) with hydroiodic acid (HI) (57 wt % in water) under a nitrogen atmosphere at 0 °C for 2 h. A white-colored powder was formed after evaporation in a rotary evaporator. The precipitate was washed several times with diethyl ether and dried under a vacuum overnight at 60 °C, then used without further purification. The synthesized $\text{CH}_3\text{NH}_3\text{I}$ (0.1975 g) and PbI_2 (0.578 g, 99% Aldrich) were mixed in dimethylformamide (1 mL, 99.8% Aldrich) overnight at 60 °C and filtered with a PTFE filter with a 0.45 μm pore size before use. To deposit the perovskite inside the gap, we spun 50 μL on top of the device at 2000 rpm for 60 s before being annealed at 90 °C for 30 min, all inside a drybox. Prior to the electrical measurements, the contacts were cleaned thoroughly with ethanol to dissolve any residues of perovskite that might interfere with the experiment. A programmable automated system mediated between an array of eight white LEDs used for illumination and a potentiostat (Autolab), with all measurements performed under a flow of nitrogen. The perovskite morphology images were acquired by a field-emission, FEI, Helios 600 high-resolution scanning electron microscope (HRSEM).

DFT calculations with periodic boundary conditions were performed. The PBE exchange-correlation functional⁴² was used for all DFT calculations. Geometry optimizations and electronic structure analysis have been carried out using the PWSCF code as implemented Quantum Espresso program package.⁴³ Electron–ion interactions were described by PBE ultrasoft pseudopotentials with electrons from Pb 5d, 6s, 6p; N and C 2s, 2p; H 1s; and I 5s, 5p shells explicitly included in the calculations. A 4 \times 4 \times 4 Monkhorst–Pack⁴⁴ grid was chosen for sampling the Brillouin zone. Plane-wave basis-set cutoffs for the smooth part of the wave functions and the augmented density of 25 and 200 Ry, respectively, were used.

■ ASSOCIATED CONTENT

§ Supporting Information

Additional HRSEM images of MAPbI_3 deposited on a gap system without an alumina top layer, decay plots with an applied bias of 1 V, and logarithmic time-scale current decay plots. This material is available free of charge via the Internet at <http://pubs.acs.org>.

■ AUTHOR INFORMATION

Corresponding Author

*E-mail: zabana@mail.biu.ac.il.

Author Contributions

[†]R.G. and E.H. have contributed equally to this work.

Notes

The authors declare no competing financial interest.

■ ACKNOWLEDGMENTS

We wish to thank Dr. Yafit Fleger, Mr. Moshe Feldberg and Mr. Shimon Pilo for their contribution. We thank the Israel Strategic Alternative Energy Foundation (I-SAEF) and the “Tashtiyot Program” of the Israeli Ministry of Science & Technology for funding this research. E.M and F.D.A thank CNR-EFOR and FP7-ENERGY-2010 project 261920 “ESCORT” for financial support. Fellowships for R.G and L.G from the Rieger-JNF Fellowship and the European Union Seventh Framework Program Destiny Project, under grant 316494 are acknowledged.

■ REFERENCES

- (1) Kojima, A.; Teshima, K.; Shirai, Y.; Miyasaka, T. Organometal Halide Perovskites as Visible-Light Sensitzers for Photovoltaic Cells. *J. Am. Chem. Soc.* **2009**, *131*, 6050–6051.
- (2) Lee, M. M.; Teuscher, J.; Miyasaka, T.; Murakami, T. N.; Snaith, H. J. Efficient Hybrid Solar Cells Based on Meso-Superstructured Organometal Halide Perovskites. *Science* **2012**, *338*, 643–647.
- (3) Burschka, J.; Pellet, N.; Moon, S.-J.; Humphry-Baker, R.; Gao, P.; Nazeeruddin, M. K.; Gratzel, M. Sequential Deposition as a Route to High-Performance Perovskite-Sensitized Solar Cells. *Nature* **2013**, *499*, 3–7.
- (4) Liu, M.; Johnston, M. B.; Snaith, H. J. Efficient Planar Heterojunction Perovskite Solar Cells by Vapour Deposition. *Nature* **2013**, *501*, 395–398.
- (5) Gottesman, R.; Tirosh, S.; Barad, H.-N.; Zaban, A. Direct Imaging of the Recombination/Reduction Sites in Porous TiO_2 Electrodes. *J. Phys. Chem. Lett.* **2013**, *4*, 2822–2828.
- (6) Kamat, P. V. TiO_2 Nanostructures: Recent Physical Chemistry Advances. *J. Phys. Chem. C* **2012**, *116*, 11849–11851.
- (7) Colella, S.; Mosconi, E.; Fedeli, P.; Listorti, A.; Gazzola, F.; Orlandi, F.; Ferro, P.; Besagni, T.; Rizzo, A.; Calestani, G.; et al. $\text{MAPbI}_{3-x}\text{Cl}_x$ Mixed Halide Perovskite for Hybrid Solar Cells: The Role of Chloride as Dopant on the Transport and Structural Properties. *Chem. Mater.* **2013**, *25*, 4613–4618.
- (8) Stranks, S. D.; Eperon, G. E.; Grancini, G.; Menelaou, C.; Alcocer, M. J. P.; Leijtens, T.; Herz, L. M.; Petrozza, A.; Snaith, H. J. Electron-Hole Diffusion Lengths Exceeding 1 Micrometer in an Organometal Trihalide Perovskite Absorber. *Science* **2013**, *342*, 341–344.
- (9) Gonzalez-Pedro, V.; Juárez-Pérez, E. J.; Arsyad, W.-S.; Barea, E. M.; Fabregat-Santiago, F.; Mora-Sero, I.; Bisquert, J. General Working Principles of $\text{CH}_3\text{NH}_3\text{PbX}_3$ Perovskite Solar Cells. *Nano Lett.* **2014**, *14*, 888–893.
- (10) Kamat, P. V. Organometal Halide Perovskites for Transformative Photovoltaics. *J. Am. Chem. Soc.* **2014**, *136*, 3713–3714.
- (11) Christians, J. A.; Fung, R. C. M.; Kamat, P. V. An Inorganic Hole Conductor for Organo-Lead Halide Perovskite Solar Cells. Improved Hole Conductivity with Copper Iodide. *J. Am. Chem. Soc.* **2014**, *136*, 758–764.
- (12) Giorgi, G.; Fujisawa, J.-I.; Segawa, H.; Yamashita, K. Small Photocarrier Effective Masses Featuring Ambipolar Transport in Methylammonium Lead Iodide Perovskite: A Density Functional Analysis. *J. Phys. Chem. Lett.* **2013**, *4*, 4213–4216.
- (13) Bisquert, J. Nano-Enabled Photovoltaics. Progress in Materials and Methodologies. *J. Phys. Chem. Lett.* **2013**, *4*, 1051–1052.
- (14) Heo, J. H.; Im, S. H.; Noh, J. H.; Mandal, T. N.; Lim, C.-S.; Chang, J. A.; Lee, Y. H.; Kim, H. J.; Sarkar, A.; Nazeeruddin, M. K.; et al. Efficient Inorganic–Organic Hybrid Heterojunction Solar Cells Containing Perovskite Compound and Polymeric Hole Conductors. *Nat. Photonics* **2013**, *7*, 486–491.
- (15) Etgar, L.; Gao, P.; Xue, Z.; Peng, P.; Chandiran, A. K.; Liu, B.; Nazeeruddin, M. K.; Gratzel, M. Mesoscopic $\text{CH}_3\text{NH}_3\text{PbI}_3/\text{TiO}_2$ Heterojunction Solar Cells. *J. Am. Chem. Soc.* **2012**, *134*, 17396–17399.
- (16) Laban, W. A.; Etgar, L. Depleted Hole Conductor-Free Lead Halide Iodide Heterojunction Solar Cell. *Energy Environ. Sci.* **2013**, *6*, 3249–3253.
- (17) Jeng, J.-Y.; Chen, K.-C.; Chiang, T.-Y.; Lin, P.-Y.; Tsai, T.-D.; Chang, Y.-C.; Guo, T.-F.; Chen, P.; Wen, T.-C.; Hsu, Y.-J. Nickel Oxide Electrode Interlayer in $\text{CH}_3\text{NH}_3\text{PbI}_3$ Perovskite/PCBM Planar-Heterojunction Hybrid Solar Cells. *Adv. Mater.* **2014**, *26*, 4107–4113.
- (18) Xing, G.; Mathews, N.; Sun, S.; Lim, S. S.; Lam, Y. M.; Gratzel, M.; Mhaisalkar, S.; Sum, T. C. Long-Range Balanced Electron- and Hole-Transport Lengths in Organic-Inorganic $\text{CH}_3\text{NH}_3\text{PbI}_3$. *Science* **2013**, *342*, 344–347.
- (19) Park, N.-G. Organometal Perovskite Light Absorbers Toward a 20% Efficiency Low-Cost Solid-State Mesoscopic Solar Cell. *J. Phys. Chem. Lett.* **2013**, *4*, 2423–2429.
- (20) Snaith, H. J. Perovskites: The Emergence of a New Era for Low-Cost, High-Efficiency Solar Cells. *J. Phys. Chem. Lett.* **2013**, *4*, 3623–3630.
- (21) Edri, E.; Kirmayer, S.; Kulpak, M.; Hodes, G.; Cahen, D. Chloride Inclusion and Hole Transport Material Doping to Improve Methyl Ammonium Lead Bromide Perovskite-Based High Open-Circuit Voltage Solar Cells. *J. Phys. Chem. Lett.* **2014**, *5*, 429–433.
- (22) Edri, E.; Kirmayer, S.; Henning, A.; Mukhopadhyay, S.; Gartsman, K.; Rosenwaks, Y.; Hodes, G.; Cahen, D. Why Lead Methylammonium Tri-Iodide Perovskite-Based Solar Cells Require a Mesoporous Electron Transporting Scaffold (but Not Necessarily a Hole Conductor). *Nano Lett.* **2014**, *14*, 1000–1004.
- (23) Barnea-Nehoshtan, L.; Kirmayer, S.; Edri, E.; Hodes, G.; Cahen, D. Surface Photovoltage Spectroscopy Study of Organo-Lead Perovskite Solar Cells. *J. Phys. Chem. Lett.* **2014**, *5*, 2408–2413.
- (24) Stoumpos, C. C.; Malliakas, C. C.; Kanatzidis, M. G. Semiconducting Tin and Lead Iodide Perovskites with Organic Cations: Phase Transitions, High Mobilities, and near-Infrared Photoluminescent Properties. *Inorg. Chem.* **2013**, *52*, 9019–9038.
- (25) Snaith, H. J.; Abate, A.; Ball, J. M.; Eperon, G. E.; Leijtens, T.; Noel, N. K.; Stranks, S. D.; Wang, J. T.-W.; Wojciechowski, K.; Zhang, W. Anomalous Hysteresis in Perovskite Solar Cells. *J. Phys. Chem. Lett.* **2014**, *5*, 1511–1515.
- (26) Baikie, T.; Fang, Y.; Kadro, J. M.; Schreyer, M.; Wei, F.; Mhaisalkar, S. G.; Gratzel, M.; White, T. J. Synthesis and Crystal Chemistry of the Hybrid Perovskite $(\text{CH}_3\text{NH}_3)\text{PbI}_3$ for Solid-State Sensitised Solar Cell Applications. *J. Mater. Chem. A* **2013**, *1*, 5628–5641.
- (27) Knop, O.; Wasylisen, R. R.; White, M. A.; Cameron, T. S.; Oort, M. J. M. Van. Alkylammonium Lead Halides. Part 2. $\text{CH}_3\text{NH}_3\text{PbX}_3$ ($X=\text{Cl}, \text{Br}, \text{I}$) Perovskites: Cubooctahedral Halide Cages with Isotropic Cation Reorientation. *Can. J. Chem.* **1990**, *68*, 412–422.
- (28) Poglitsch, A.; Weber, D. Dynamic Disorder in Methylammoniumtrihalogenoplumbates (II) Observed by Millimeter-Wave Spectroscopy. *J. Chem. Phys.* **1987**, *87*, 6373–6378.
- (29) Mosconi, E.; Amat, A.; Nazeeruddin, M. K.; Gratzel, M.; De Angelis, F. First-Principles Modeling of Mixed Halide Organometal

Perovskites for Photovoltaic Applications. *J. Phys. Chem. C* **2013**, *117*, 13902–13913.

(30) Kawamura, Y.; Mashiyama, H.; Hasebe, K. Structural Study on Cubic-Tetragonal Transition of $\text{CH}_3\text{NH}_3\text{PbI}_3$. *J. Phys. Soc. Jpn.* **2002**, *71*, 1694–1697.

(31) Even, J.; Pedesseau, L.; Jancu, J.-M.; Katan, C. Importance of Spin–Orbit Coupling in Hybrid Organic/Inorganic Perovskites for Photovoltaic Applications. *J. Phys. Chem. Lett.* **2013**, *4*, 2999–3005.

(32) Amat, A.; Mosconi, E.; Ronca, E.; Quarti, C.; Umari, P.; Nazeeruddin, M. K.; Graetzel, M.; De Angelis, F. Cation-Induced Band-Gap Tuning in Organohalide Perovskites: Interplay of Spin–Orbit Coupling and Octahedra Tilting. *Nano Lett.* **2014**, *14*, 3608–3616.

(33) Umari, P.; Mosconi, E.; De Angelis, F. Relativistic GW Calculations on $\text{CH}_3\text{NH}_3\text{PbI}_3$ and $\text{CH}_3\text{NH}_3\text{SnI}_3$ Perovskites for Solar Cell Applications. *Sci. Rep.* **2014**, *4*, 4467.

(34) Brivio, F.; Butler, K. T.; Walsh, A.; Schilfgaarde, M. Van. Relativistic Quasiparticle Self-Consistent Electronic Structure of Hybrid Halide Perovskite Photovoltaic Absorbers. *Phys. Rev. B* **2014**, *90*, 155204.

(35) Brivio, F.; Walker, A. B.; Walsh, A. Structural and Electronic Properties of Hybrid Perovskites for High-Efficiency Thin-Film Photovoltaics from First-Principles. *Appl. Phys. Lett.* **2013**, *103*, 042111–1.

(36) Even, J.; Pedesseau, L.; Katan, C. Analysis of Multivalley and Multibandgap Absorption and Enhancement of Free Carriers Related to Exciton Screening in Hybrid Perovskites. *J. Phys. Chem. C* **2014**, *118*, 11566–11572.

(37) Choi, J. J.; Yang, X.; Norman, Z. M.; Billinge, S. J. L.; Owen, J. S. Structure of Methylammonium Lead Iodide Within Mesoporous Titanium Dioxide: Active Material in High-Performance Perovskite Solar Cells. *Nano Lett.* **2013**, *14*, 127–133.

(38) Dualeh, A.; Moehl, T.; Tetreault, N.; Teuscher, J.; Gao, P.; Nazeeruddin, M. K.; Gratzel, M. Impedance Spectroscopic Analysis of Lead-Iodide Perovskite-Sensitized Solid-State Solar Cells. *ACS Nano* **2014**, *8*, 362–373.

(39) Sanchez, R. S.; Gonzalez-Pedro, V.; Lee, J.-W.; Park, N.-G.; Kang, Y. S.; Mora-Sero, I.; Bisquert, J. Slow Dynamic Processes in Lead Halide Perovskite Solar Cells. Characteristic Times and Hysteresis. *J. Phys. Chem. Lett.* **2014**, *5*, 2357–2363.

(40) Juarez-Perez, E. J.; Sanchez, R. S.; Badia, L.; Garcia-Belmonte, G.; Kang, Y. S.; Mora-Sero, I.; Bisquert, J. Photoinduced Giant Dielectric Constant in Lead Halide Perovskite Solar Cells. *J. Phys. Chem. Lett.* **2014**, *5*, 2390–2394.

(41) Kim, H.-S.; Lee, C.-R.; Im, J.-H.; Lee, K.-B.; Moehl, T.; Marchioro, A.; Moon, S.-J.; Humphry-Baker, R.; Yum, J.-H.; Moser, J. E.; et al. Lead Iodide Perovskite Sensitized All-Solid-State Submicron Thin Film Mesoscopic Solar Cell with Efficiency Exceeding 9%. *Sci. Rep.* **2012**, *2*, 591.

(42) Perdew, J. P.; Burke, K.; Ernzerhof, M. Generalized Gradient Approximation Made Simple. *Phys. Rev. Lett.* **1996**, *77*, 3865–3868.

(43) Giannozzi, P.; Baroni, S.; Bonini, N.; Calandra, M.; Car, R.; Cavazzoni, C.; Ceresoli, D.; Guido, L. C.; Cococcioni, M.; Dabo, I.; et al. QUANTUM ESPRESSO: A Modular and Open-Source Software Project for Quantum Simulations of Materials. *J. Phys.: Condens. Matter* **2009**, *21*, 395502.

(44) Monkhorst, H. J.; Pack, J. D. Special Points for Brillouin-Zone Integrations. *Phys. Rev. B* **1976**, *13*, 5188–5192.